

SiO_x Gas Barrier Coatings on Polymer Substrates: Morphology and Gas Transport Considerations

A. G. Erlat[†] and R. J. Spontak^{*}

*Departments of Materials Science & Engineering and Chemical Engineering,
North Carolina State University, Raleigh, North Carolina 27695*

R. P. Clarke, T. C. Robinson, P. D. Haaland, Y. Tropsha, N. G. Harvey, and E. A. Vogler[§]

*Polymer Science & Technology Department, Becton Dickinson Technologies,
Research Triangle Park, North Carolina 27709*

Received: March 2, 1999; In Final Form: May 4, 1999

Plasma-enhanced chemical vapor deposition (PECVD) of SiO_x thin coatings on polymer surfaces yields tough hybrid materials with the gas barrier properties and transparency of glass. Combination of these properties makes these materials ideally suited for food packaging and biomedical device applications. In this study, we employ a Non-Parametric Response Surface Methods optimization to identify the Magnetron-PECVD conditions responsible for superlative SiO_x barrier coatings on poly(ethylene terephthalate) (PET). Oxygen and water vapor permeances of optimized PET/SiO_x composites produced by hexamethyldisiloxane and trimethylsilane have been measured as functions of temperature and are found to exhibit Arrhenius behavior. The thermal activation energy for water vapor permeation, unlike that for oxygen permeation, depends on barrier performance and increases by as much as 20 kJ/mol with an increase in barrier efficacy. Examination of these materials by phase-imaging atomic force microscopy and energy-filtered transmission electron microscopy reveals a correlation between SiO_x morphology (including defects) and barrier performance. Morphological and permeation results are compared to identify some of the physical factors governing water vapor permeation through SiO_x-modified polymers.

Introduction

Over the past decade, interest in transparent, thin SiO_x barrier coatings deposited on polymer substrates has increasingly grown in the food packaging and medical device industries.¹ Such coatings possess highly desirable properties, such as transparency, recyclability, retortability, and microwave use,^{1–3} and are superior in these regards to the thin metal (generally aluminum-based⁴) coatings currently employed commercially on various polymer substrates. For the SiO_x coatings to compete effectively against more established, as well as concurrently emerging,^{5–7} barrier technologies, they must demonstrate time and temperature stability and promote substantially reduced oxygen and water vapor permeability. Recent studies^{2,8,9} of SiO_x coatings produced by different processing routes have, in fact, shown that both of these criteria are satisfied. One of the benefits of these coatings lies in the flexibility by which they can be deposited on polymer surfaces. Thus far, sputtering,^{10,11} electron-beam deposition,^{1,2} and plasma-enhanced chemical vapor deposition (PECVD)^{8,10,12,13} have all been utilized successfully to produce SiO_x barrier coatings on polymer substrates. Of these methods, the latter has become the most popular due to its operational ease and efficacy, as signified by low-temperature deposition, improved coverage, and process tunability.^{14,15}

Previous studies^{11,12} of SiO_x coatings have, for the most part, concentrated on reporting improvements in (i) measured oxygen and water vapor permeabilities and (ii) the design of high-vacuum deposition systems. To improve the quality of these coatings, however, it is crucial to identify and understand the correlation between barrier performance, morphological characteristics, and molecular transport, which may all be governed by the deposition conditions.

Surface and subsurface characterization of SiO_x coatings by atomic force microscopy (AFM)^{16–21} and scanning electron microscopy (SEM)^{21–23} reveals that the surface of such coatings can be described as columnar or granular. Roughness measurements performed^{20,21} by AFM have likewise shown that permeability generally decreases with increasing surface smoothness. In light of these results, the principal structure of the coating regulating permeation is currently believed to consist of fine-scale (Ångstrom- or nanometer-level) defects, instead of pores in the micrometer range.²³ Such fine-scale defects induce highly tortuous molecular-size pathways through which penetrant molecules must diffuse before reaching the polymer substrate. Prior attempts^{22,24} to examine these defects by cross-sectional high-resolution transmission electron microscopy (TEM) have met with limited success due to difficulties associated with sample preparation and defect identification. As a complement to morphological characterization, permeation activation energy measurements of SiO_x coatings on several commodity polymer substrates have been conducted by Tropsha and Harvey.²⁵ To explain observed data trends, their study proposes a simplified defect model, which provides valuable insight into the mech-

^{*} To whom correspondence should be addressed (Rich_Spontak@ncsu.edu).

[†] Present address: Department of Materials, University of Oxford, Oxford OX1 3PH, United Kingdom.

[§] Present address: Department of Materials Science & Engineering, The Pennsylvania State University, University Park, Pennsylvania 16802.

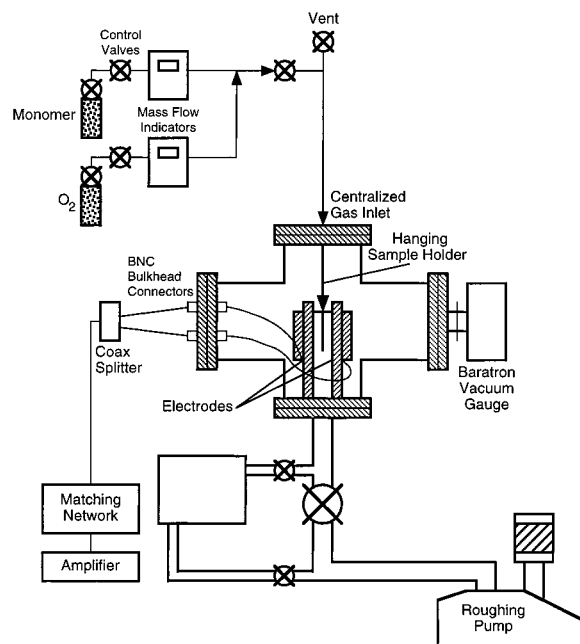


Figure 1. Schematic diagram of the Magnetron-PECVD system employed in this study to deposit SiO_x on poly(ethylene terephthalate) (PET) substrates.

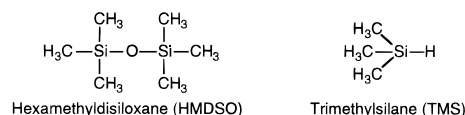
anism (in terms of molecular tortuosity) dictating oxygen and water vapor permeation through the coatings. Recent results reported by Henry et al.²⁴ combine morphological and activation energy measurements obtained for a variety of gases, and support the existence of fine-scale defects varying in size and density (thereby affecting barrier performance).

In the present study, the extensive statistical Non-Parametric Response Surface Methods (NPRSM) algorithm²⁶ has been applied to optimize Magnetron-PECVD and obtain superior quality SiO_x barrier coatings deposited on poly(ethylene terephthalate) (PET) substrates. Results acquired from this experimental design facilitate comparison of coating microstructure, surface morphology, and gas (oxygen and water vapor) transport mechanisms of SiO_x coatings differing in barrier performance to identify statistically meaningful correlations. Moreover, planar, rather than cross-sectional, TEM is used to resolve the fine-scale defects in the SiO_x films just alluded to, whereas AFM provides insight into the growth mechanism and texture evolution of the coatings. Temperature-dependent permeation measurements obtained from oxygen and water vapor transport are analyzed in the context of thermally activated rate theory, and the results are discussed here in light of the morphological characteristics discerned by TEM and AFM.

Experimental Section

Material Processing. The PET employed in this study was obtained in sheet form from Atlantic Plastics (Raleigh, NC) and had a number-average molecular weight of 38 000. It was extruded into a thin (25 μm thick) film, which was about 28% crystalline, according to differential scanning calorimetry measurements. The SiO_x coatings investigated here were deposited on this PET film, cut into 8 cm \times 8 cm squares, at room temperature in a Magnetron, a magnetically enhanced PECVD apparatus schematically depicted in Figure 1 and described in detail elsewhere.²⁷ In the Magnetron, a magnetic field was superimposed on the 10 cm \times 10 cm titanium vertical electrodes by placing 10 bar magnets radially on the backside of each electrode, and two PET films sandwiched together were

SCHEME 1



suspended symmetrically between the anode and cathode. Following this, the chamber was evacuated to below 1 Torr using a roughing pump, whereupon the turbomolecular pump was activated. At this point, the flow rates of monomer and oxidizer, as well as the pressure, were adjusted. Upon system stabilization over the course of few minutes, the electrodes were energized, and the matching network was tuned to a predetermined power level. The deposition time was maintained constant at 3 min, after which time the power was turned off for a brief cool-down period. This process was repeated twice more for a total of three 3-min depositions/sample. At the end of this deposition sequence, the chamber was vented and the two coated samples were carefully removed for testing. From AFM and cross-sectional SEM analyses, the coatings typically ranged from about 20 to 200 nm in thickness, depending on their quality.

Two coating series were produced by feeding trimethylsilane (TMS) and hexamethyldisiloxane (HMDSO) monomers, supplied at 98% purity from United Chemical Technologies and Aldrich Chemicals (Milwaukee, WI), respectively, into the plasma chamber with O_2 at 99.5% purity from National Welders (Raleigh, NC). The chemical structures of the SiO_x -forming monomers are displayed in Scheme 1. In each series, three important deposition parameters — power, oxygen flow rate and monomer flow rate — were varied according to results from the NPRSM optimization to operate at optimum process conditions and ensure superior barrier performance.

Material Characterization. Oxygen transmission measurements were performed over the course of 24 h on an Oxtran 2/20 permeability testing instrument (Modern Controls, Inc., Minneapolis, MN) at 10, 20, 30, 35, and 40 °C. Water vapor transmission rates were measured under analogous conditions from 24 to 38 °C with a Permatran W600 (Modern Controls, Inc.). A Digital Instruments Nanoscope D-3000 operated in tapping mode²⁸ provided phase and topographical images of SiO_x coatings, as well as corresponding root-mean-square (rms) surface roughness measurements. Complementary TEM analysis was conducted on the SiO_x coatings by using a method developed⁴ for the examination of metallized Al coatings deposited on PET. Small pieces of the PET/ SiO_x composites were placed on 400-mesh copper TEM grids, and the grids were arranged on a graphite screen elevated by metal supports in a Petri dish. Upon addition of *o*-chlorophenol, the dish was covered and heated to 110 °C, which resulted in complete dissolution of the PET substrate over the course of 1 h. [The lid was removed every 10 min in a fumehood to avoid condensation of *o*-chlorophenol vapor on the fragile SiO_x film.] The resulting self-supported SiO_x film was imaged on a Zeiss transmission electron spectroscopic microscope operated at 80 kV in zero-loss ($\Delta E = 0$ eV) imaging mode²⁹ to enhance phase contrast (by filtering out the inelastically scattered electrons responsible for image noise).

Results and Discussion

Process Parameters. The NPRSM experimental design facilitates identification of the optimum settings of the Magnetron-PECVD process parameters responsible for minimizing oxygen permeation through the PET/ SiO_x composites. The

TABLE 1: Magnetron-PECVD Deposition Settings Obtained from the NPRSM Optimization

monomer	settings	power (W)	O ₂ flow rate (sccm)	monomer flow rate (sccm)
HMDSO	initial	23–40	0.5–4.0	3.0–10
	optimal	65	6.5	15.5
TMS	initial	20–45	0.8–4.2	2.5–11
	optimal	65	7.0	15.0

experimental variables optimized during the course of this extensive statistical design include deposition power, expressed in watts, and the monomer and oxygen flow rates, both expressed in units of cm³(STP)/min (hereafter abbreviated sccm for consistency with the literature). These are considered^{13,26} to constitute the crucial process parameters governing film quality in a PECVD process. Additional conditions, such as deposition time and cool between depositions, have been held constant to ensure valid material comparison, whereas pressure and signal frequency are adjusted according to the optimum parameters selected.

Process optimization is conducted separately for films coated with HMDSO and TMS monomers. Throughout this optimization, reactor constraints and process modifications define the experimental boundaries at each step of the experimental design. The optimization strategy for both monomers starts with a fractional factorial design, developed on the basis of previous information regarding the Magnetron-PECVD system,³⁰ as the feasible operating regime. Initial conditions are listed in Table 1. Identification of these initial conditions is followed by fractional factorial designs, steepest ascent pathways, response surface designs, space-filling designs, and optimum search algorithms that all employ thin-spline models.³¹ A detailed review providing the sequence of experiments resulting in this experimental design is available elsewhere.²⁵ During the course of optimization, a reduction in oxygen transmission rate (Π_{O_2}) is accompanied by increases in all three PECVD process parameters from their initial settings, thereby enabling construction of the comprehensive process map displayed in Figure 2. Here, contour plots corresponding to the three optimum process conditions for films deposited from HMDSO are displayed. Similar contour plots have been generated for the TMS monomer, but are not included here because the HMDSO-based coatings were studied more extensively (thereby yielding a more complete optimization picture).

The effect of simultaneously varying power and HMDSO flow rate on Π_{O_2} is shown at a constant O₂ flow rate of 6.5 sccm in Figure 2a. At the optimum HMDSO flow rate (ca. 15.5 sccm), the contour lines reveal a significant improvement in barrier performance (i.e., reduced Π_{O_2}) as the power level is increased. A bowl-shaped optimum in the vicinity of 65 W is eventually realized. This behavior is attributed to a more intense plasma in the glow region and a corresponding increase in the kinetic energy of ions, resulting in enhanced ion bombardment, which improves the degree to which HMDSO and O₂ molecules dissociate to form dense and uniform SiO_x networks.³² Moreover, oxidation of elements such as carbon and hydrogen is complete under these conditions.^{27,32} This constitutes an important consideration, because unwanted byproduct gases (e.g., CO, CO₂, and H₂O) are formed at this power level and subsequently vented out of the plasma chamber, minimizing the level of impurities incorporated within the SiO_x coating.

As is also evident in Figure 2a, higher or lower HMDSO flow rates promote a significant (and highly undesirable) increase in Π_{O_2} . An insufficient HMDSO flow rate at any power level is expected to generate poor SiO_x coatings due to premature

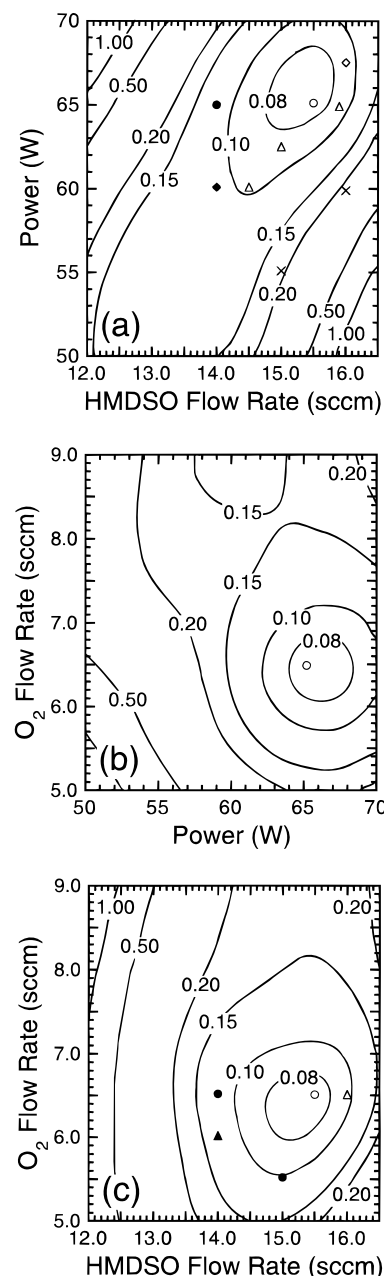


Figure 2. Contour plots of oxygen transmission rate (Π_{O_2} , in cm³/m²-atm-day) resulting from the Non-Parametric Response Surface Methods (NPRSM) optimization in which the following parameters are fixed: (a) O₂ flow rate (6.5 sccm), (b) HMDSO flow rate (15.5 sccm) and (c) deposition power (65 W). To demonstrate the sensitivity of Π_{O_2} on processing, several experimental Π_{O_2} data are included: 0.07 (○), 0.08 (△), 0.09 (◇), 0.10 (●), 0.12 (▲), 0.14 (◆) and 0.23 (×).

monomer depletion, which would become more pronounced with increasing power (and HMDSO consumption). Premature HMDSO depletion would, in turn, result in incomplete surface coverage, nonuniform coating thickness and more defect sites, thereby increasing Π_{O_2} . Excess monomer at high HMDSO flow rates (particularly at low power levels), on the other hand, would leave unreacted species in the chamber upon plasma deactivation. These species would tend to deposit on the SiO_x coating if they did not vent out of the chamber during deposition. The presence of such impurities in SiO_x coatings can be highly detrimental to the coating chemistry and, hence, increase gas permeability.³³

For comparison, Figure 2b displays the effect of varying power and O₂ flow rate on Π_{O_2} at a constant HMDSO flow

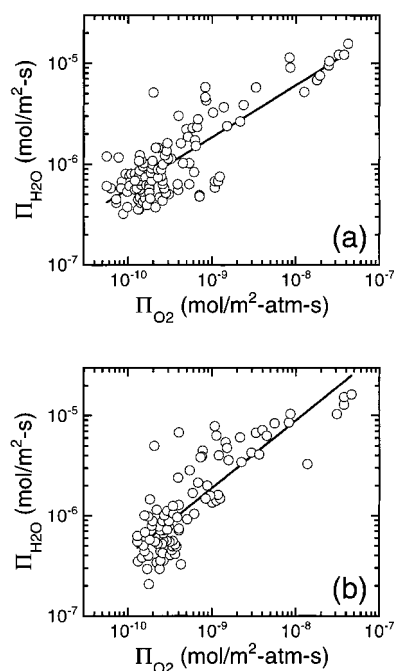


Figure 3. Variation of the water vapor transmission rate (Π_{H_2O}) with oxygen transmission rate (Π_{O_2}) on double-logarithmic coordinates for SiO_x -coated PET in which the SiO_x layer is derived from (a) HMDSO and (b) TMS monomer. The solid line is a power-law fit to the data.

rate of 15.5 sccm. The role of power is the same as that already discussed with regard to Figure 2a. At the optimum power level (ca. 65 W), a bowl-shaped minimum in Π_{O_2} is apparent, centered at an O_2 flow rate of about 6.5 sccm. Reduction in barrier performance at higher and lower O_2 flow rates can be explained in terms of coating properties. At higher O_2 flow rates, the SiO_x coatings possess a higher oxygen content and become brittle (and prone to stress cracking).³ Lower O_2 flow rates produce porous SiO_x coatings with a high carbon content, because the byproduct gases mentioned earlier would not form completely and vent during deposition.³² Figure 2c represents the combinatorial effect of concurrently varying HMDSO and O_2 flow rates on Π_{O_2} at a constant power level of 65 W. As in the two previous figures, a minimum in Π_{O_2} is resolved at HMDSO and O_2 flow rates of about 15.5 and 6.5 sccm, respectively. At a constant O_2 flow rate, the barrier efficacy of SiO_x coatings degrades upon increasing or decreasing the HMDSO flow rate. At low flow rates, the formation of SiO_x networks is hindered (despite plasma activation) due to HMDSO depletion, yielding nonuniform and insufficiently dense coatings. For the opposite case of excess HMDSO monomer, impurities again contaminate the SiO_x coatings.

In the previous section, results from the NPRSM optimization have been compared with limited experimental data to show that subtle changes in Magnetron-PECVD deposition parameters could induce dramatic, and undesirable, increases in Π_{O_2} . A design consideration to be addressed at this juncture is whether the optimization parameters identified in Figure 2 for Π_{O_2} could be legitimately extended to water vapor. This uncertainty is resolved in Figure 3a, in which water vapor transmission rate (Π_{H_2O}) is presented as a function of Π_{O_2} for various SiO_x -coated PET samples produced under different deposition conditions. Although these data exhibit scatter, they nonetheless demonstrate that an increase in Π_{O_2} is accompanied by an increase in Π_{H_2O} (the correlation coefficient for the solid line shown in this figure is 0.92). Such correlation confirms that, although oxygen and water vapor possess vastly different properties (e.g., water vapor

is highly condensable), (i) SiO_x coatings constitute excellent barrier materials against both permeants, and (ii) the optimization results discussed earlier with respect to Π_{O_2} may be applied, at least semiquantitatively, to Π_{H_2O} .

The data compiled in Table 1 reveal that the optimum parameter settings for HMDSO and TMS are nearly identical, suggesting that the barrier performance of SiO_x coatings produced from both monomers is comparable. This inference is supported by the data provided in Figure 3b. Here, Π_{H_2O} is shown as a function of Π_{O_2} for PET/ SiO_x composites in which the SiO_x coating is derived from TMS monomer. Comparison of Figures 3a and 3b reveals that (i) the Π_{H_2O} - Π_{O_2} correlation identified for coatings from HMDSO is valid for those generated from TMS, and (ii) coatings that exhibit similar barrier performance can be obtained from either HMDSO or TMS. This last point is in agreement with prior studies¹ in which different organosilicon monomers did not significantly influence the barrier efficacy of the resultant SiO_x coatings. [The apparent improvement in coatings from HMDSO may reflect, in part, the more extensive HMDSO analysis alluded to earlier.] In comparing Π_{O_2} and Π_{H_2O} data from the same specimens (as is done in Figure 3), an important point to note is that O_2 measurement was performed prior to H_2O measurement for two reasons. First, O_2 constitutes a better model permeant because of its established and relatively simplistic transport properties. For this reason, it is often employed in studies of barrier coatings,¹⁻¹³ whereas water vapor permeation can be problematic due to the preponderance of water molecules to hydrogen-bond in highly confined or porous environments.³⁴ The second reason for measuring Π_{O_2} before Π_{H_2O} is that water vapor is known³⁵ to induce structural changes in SiO_x through stress cracking.

Morphological Characteristics. Atomic force microscopy has been employed in this study to identify (and quantify where possible) differences arising in surface morphology and roughness from samples exhibiting barrier efficacies ranging from 10 to 167 \times improvement in Π_{O_2} relative to the uncoated PET substrate ($\Pi_{O_2} = 80 \text{ cm}^3/\text{m}^2\text{-atm-day}$). For this comparison, samples with SiO_x coatings produced from the TMS monomer have been selected along the Π_{H_2O} - Π_{O_2} correlation shown in Figure 3b. Images collected from $5 \mu\text{m} \times 5 \mu\text{m}$ areas do not reveal macroscopic defects, such as pinholes or macropores, on the SiO_x coating surface, which is in agreement with results reported by Garcia-Ayuso et al.,¹⁶ who confirmed that pinholes cannot be fully responsible for measured permeabilities through SiO_x coatings. The absence of defects also reflects the relatively low Π_{O_2} values measured from the chosen samples ($0.48\text{--}7.8 \text{ cm}^3/\text{m}^2\text{-atm-day}$). To ascertain if morphological features are at least partly responsible for the differences in Π_{O_2} , higher resolution $1 \mu\text{m} \times 1 \mu\text{m}$ phase and oblique (3-D) images are presented in Figure 4. These images are representative of the surfaces and clearly show differences in the surface texture (and growth mechanism) of SiO_x coatings varying in barrier quality.

The phase images displayed in Figure 4 are similar in appearance to those obtained by Wang et al.¹⁹ for SiO_x coatings derived from HMDSO monomer on polystyrene and polycarbonate substrates. Deposited near optimum PECVD conditions, the best coating is displayed in Figure 4a. Its surface consists of densely packed, spherical clusters of SiO_x networks (grains) with well-defined boundaries. The majority (75–80% of the total image area) of these features measure $24 \pm 4 \text{ nm}$, with larger features measuring $56 \pm 13 \text{ nm}$ distributed randomly. Such fine uniform features are responsible for the low Π_{O_2} measured ($0.48 \text{ cm}^3/\text{m}^2\text{-atm-day}$) because the penetrant mol-

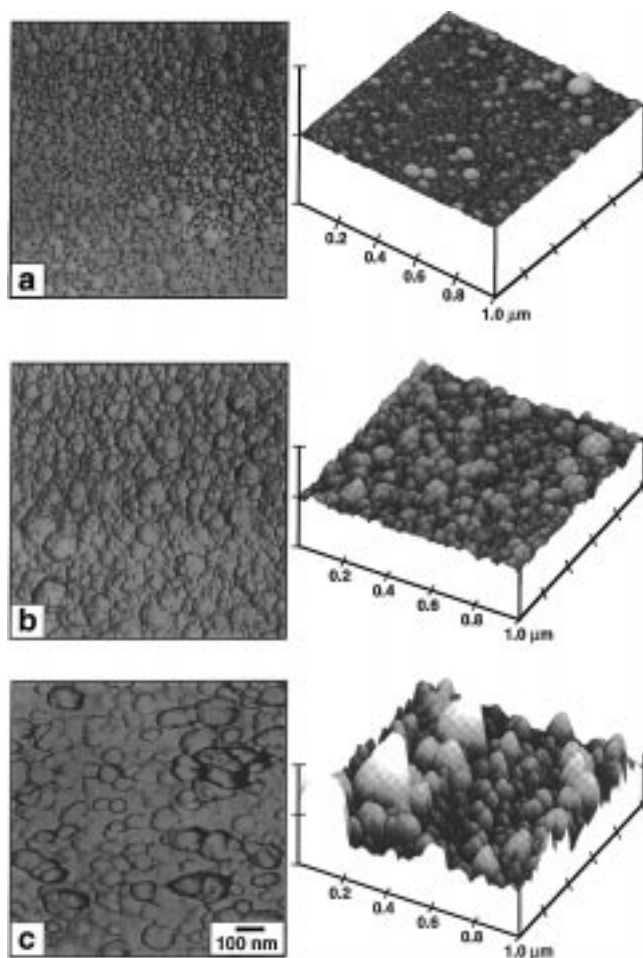


Figure 4. Atomic force microscopy images obtained in tapping mode from SiO_x coatings exhibiting different levels of barrier performance, as measured in terms of O₂ transmission rate (Π_{O_2} , in cm³/m²-atm-day): (a) 0.48, (b) 1.5, and (c) 7.8. Each height division corresponds to 100 nm.

ecules locate and diffuse through the relatively few and small defect sites (due to the dense packing of particles) within the coating. As the deposition conditions deviate slightly from optimum, a poorer barrier coating ($\Pi_{O_2} = 1.5$ cm³/m²-atm-day) is produced. The surface texture of this coating is visible in Figure 4b. Note that the shape of the SiO_x clusters is irregular with sharper grain boundaries, which may favor the formation of defect sites. Another characteristic of this figure is that the texture is composed of features that measure 37 ± 10 nm across and that appear to coalesce into larger agglomerates measuring 96 ± 16 nm in diameter. An increase in particle size is accompanied by an increase in grain boundary area. When this effect is combined with the irregular grain texture, it is anticipated that a greater number of penetrant molecules will diffuse through intergranular pores. In Figure 4c, the surface morphology of a barrier coating providing only a 10 \times improvement in barrier efficacy with respect to the uncoated PET substrate is displayed. This image reveals that relatively large and irregularly shaped particle clusters (individual particles could not be resolved) comprise the SiO_x coating, which appears to be very inhomogeneous because of nonoptimum deposition.

Insight into the permeation mechanism through PECVD-deposited SiO_x coatings can be gleaned from the oblique (3-D) topographical images included in Figure 4. The characteristic surface topography of SiO_x coatings can be described as dome-shaped, as seen in the 3-D images. Upon comparing Figures 4a–c, the domes are observed to deform and become irregular

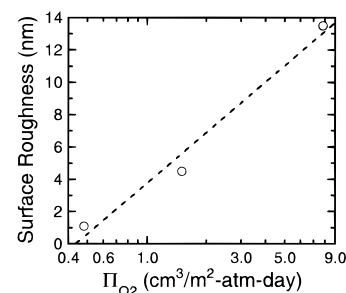


Figure 5. Values of the rms surface roughness obtained from the AFM images in Figure 4 and presented here as a function of Π_{O_2} on semilogarithmic coordinates. The dashed line is a logarithmic fit to the data and serves as a guide for the eye.

as the barrier performance degrades. When compared on a fixed vertical scale (z-range of 200 nm), the topography of the best barrier (Figure 4a) appears to be composed of uniformly distributed, small columnar features, which become larger and irregular as the barrier performance decreases (Figures 4b–c). The large domes create valleys that may not be completely covered with SiO_x, thereby forming diffusive pathways in coatings that exhibit poor barrier quality. Such megalithic structures invariably change the rms surface roughness, which is shown in Figure 5 as a function of Π_{O_2} for the AFM images provided in Figure 4. Although a direct relationship has not yet been conclusively established, the surface roughness of SiO_x coatings is believed to be a nonnegligible factor affecting barrier performance.^{20,22} Correlation between surface roughness and Π_{O_2} is evident in this figure, but more data are necessary to establish an indisputable relationship.

In the previous sections, the Π_{O_2} and Π_{H_2O} values clearly demonstrate a tremendous improvement in barrier performance relative to PET. These data nevertheless indicate that even the best SiO_x coatings are not impermeable, in which case defects (pores) create pathways through which penetrant molecules diffuse. Marked improvement in barrier efficacy, coupled with AFM results such as those presented in Figure 4, implies that the best barrier coatings are completely devoid of macropores or pinholes. Thus, the defects governing O₂ and water vapor permeation through these coatings must be pores in the nanometer or even Ångström size range. Previous attempts to identify such defects have employed cross-sectional TEM^{22,24} and planar SEM,^{21–23} but defects in this size range have not been satisfactorily resolved. In the present work, planar TEM images have been collected to discern the presence, size, and distribution of nanoscale defects in SiO_x coatings varying in barrier effectiveness. Shown in Figure 6 are energy-filtered TEM micrographs of two SiO_x coatings derived from TMS monomer with Π_{O_2} values of 0.52 and 16 cm³/m²-atm-day, which provide a comparison between good and relatively poor barrier coatings.

The microstructure corresponding to a good SiO_x barrier coating (Figure 6a) consists of spherical SiO_x particles that are tightly packed and uniformly deposited. Numerous small particles range in diameter from 20 to 30 nm, whereas fewer large particles measure 40 to 60 nm across, in agreement with the AFM image displayed in Figure 4a. The low level of contrast in the micrograph reflects the even coating thickness. Electron-opaque (dark) features distributed randomly in the images, can most likely be attributed to mass-thickness contrast due to the deposition conditions or sample preparation described earlier. It is likewise conceivable that these features represent particles that are richer in silicon (and lower in carbon) than the surrounding matrix. For superior SiO_x coatings, no intergranular pores (which would appear light in transmission) are discernible,

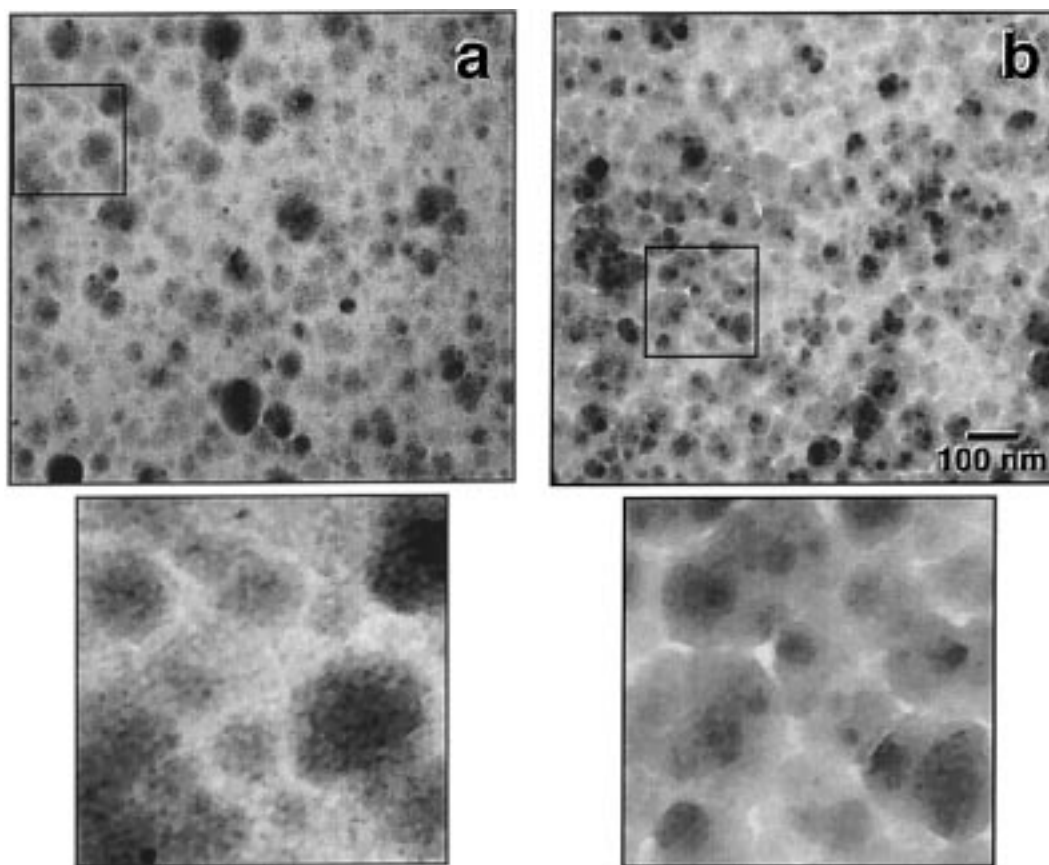


Figure 6. Energy-filtered (zero-loss) TEM images of a good SiO_x barrier coating ($\Pi_{\text{O}_2} = 0.52 \text{ cm}^3/\text{m}^2\text{-atm-day}$; a) in comparison to a poor barrier coating ($\Pi_{\text{O}_2} = 16 \text{ cm}^3/\text{m}^2\text{-atm-day}$; b). Overall contrast is relatively low in these images because of the even mass thickness and atomic composition. Enlargements reveal the presence of defects (pores) between adjacent SiO_x grains in (b). The size, shape, and density of such nanoscale defects govern gas permeation through SiO_x -coated polymers.

indicating that such defects, if they exist, measure $<1 \text{ nm}$ across (the lower limit cannot be determined with certainty due to the resolution limit of the microscope, which is estimated to be about 0.4 nm in zero-loss imaging mode). This size scale is consistent with the low Π_{O_2} obtained by depositing the coating at or near optimum conditions. Nanoscale defects are clearly resolved in the image provided in Figure 6b for a relatively poor barrier coating. The first result worth noting in this image is the gross change in microstructure, in which many of the SiO_x particles, of comparable size to those in Figure 6a, no longer appear spherical in shape. Instead, the particles in Figure 6b are deformed into irregular shapes possessing sharp boundaries. Moreover, intergranular defects account for about 30% of the sample area, and typically measure ca. $4\text{--}6 \text{ nm}$ (but, in some cases, extend up to almost 15 nm) across. Pores this large will readily accommodate a significant flux of either O_2 (molecular diameter of 0.33 nm) or water vapor (molecular diameter of 0.32 nm).³⁶

These results provide visual evidence to substantiate the hypothesis that the principal mechanism of molecular transport in the best SiO_x coatings occurs through nanoscale intergranular pores in the Angstrom or nanometer size range. Because the coating deposition deviates from the optimum process conditions listed in Table 1 and the barrier quality is degraded, the size and density of nanoscale defects increase markedly, resulting in coatings composed of irregularly shaped particles. One drawback of TEM images is that they are 2-D projections of 3-D features, in which case information regarding the precise shape of these pores through the coating is not possible without the use of transmission electron microtomography. The activa-

tion energy studies presented in the following section will, however, provide additional insight into this issue.

Permeation Measurements. The temperature dependence of ideal molecular transport through silicon oxide glasses^{37,38} and polymers below their glass transition temperature³⁹ can be generally represented by an Arrhenius equation of the form:

$$\Pi = \Pi_0 \exp(-\Delta G^\ddagger/RT) \quad (1)$$

Here, ΔG^\ddagger is the thermal activation energy, R is the universal gas constant, and T denotes absolute temperature. Equation 1, if applicable to the PET/ SiO_x composites investigated here, could be used to probe the nanostructure of the SiO_x coatings because ΔG^\ddagger should be sensitive to changes in the mechanism of molecular transport.²⁵ The transmission data displayed in Figure 3 reflect >100 samples prepared according to the NPRSM optimization and measured at 30°C . Temperature-dependent transmission (Π) measurements have been acquired from a limited series of HMDSO-based SiO_x coatings selected along the correlation included in Figure 3a, and representative data are presented in Arrhenius-type fashion for both O_2 and H_2O transmission in Figures 7a and 7b, respectively. In all cases, Arrhenius behavior is apparent, indicating that eq 1 may be applied to analyze the data collected here.

Values of $\Delta G^\ddagger_{\text{O}_2}$ determined from $\Pi_{\text{O}_2}(T)$ data are compiled in Table 2 and indicate that O_2 transmission through SiO_x -coated PET ($\Delta G^\ddagger_{\text{O}_2} = 30 \pm 2 \text{ kJ/mol}$) and uncoated PET ($\Delta G^\ddagger_{\text{O}_2} = 29 \text{ kJ/mol}$) occurs by the same mechanism, even if the barrier performance is increased by a factor of $182\times$. This result supports the results of a previous study by Tropsha and

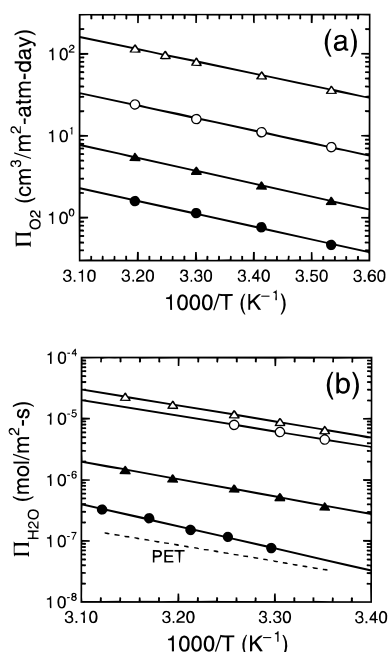


Figure 7. Dependence of (a) oxygen transmission rate (Π_{O_2}) and (b) water vapor transmission rate (Π_{H_2O}) on reciprocal temperature for four SiO_x coatings produced under various conditions to yield different barrier performance. These data are differentiated in terms of Π_{O_2} measured at 30 °C (in $\text{cm}^3/\text{m}^2\text{-atm-day}$): 0.18 (●), 1.6 (▲), 16 (○) and 80 (PET, △). The solid lines are exponential fits to the data, which exhibit Arrhenius-type temperature dependence (see eq 1). The dashed line in (b) corresponds to uncoated PET, shifted down from the data (△) to facilitate comparison with the slopes from the low- Π_{O_2} data.

TABLE 2: Representative Values of $\Delta G^\ddagger_{O_2}$ as a Function of Barrier Performance (Π_{O_2} at 30 °C)

Π_{O_2} ($\text{cm}^3/\text{m}^2\text{-atm-day}$)	$\Delta G^\ddagger_{O_2}$ (kJ/mol)
0.44	30.4
0.66	31.2
1.5	32.2
2.0	29.5
7.8	27.3
13	29.6
mean	30.0 ± 1.7

Harvey,²⁵ who proposed that the particles comprising SiO_x coatings serve as blockades that oxygen molecules must traverse to reach the PET substrate (where primary activated transport occurs). Invariance in the activation energy for O₂ transmission confirms that the SiO_x coatings, despite their enhanced barrier performance, are not defect-free, which is in agreement with the TEM images shown in Figure 6. In the present study, the Magnetron-PECVD conditions have been systematically varied to generate superlative barrier efficacy. As the barrier efficacy is increased and the size and density of defects are reduced, one might suspect the eventual existence of a permeation regime in which the size of defects in the SiO_x coating is of the same scale as the penetrant molecule. In this case, the permeant may be forced to diffuse along the axis of its smallest projected area or be otherwise constricted, thereby causing an increase in ΔG^\ddagger . Although such behavior is in fact observed⁴⁰ in SiO_x coatings produced from HMDSO by radio frequency (RF) discharge PECVD on polycarbonate, it is not evident in the Π_{O_2} data reported here because of differences in either the coatings (Magnetron-PECVD *vs.* RF-discharge PECVD) or the polymer substrates (semicrystalline *vs.* glassy).

In marked contrast, $\Delta G^\ddagger_{H_2O}$ for water vapor transmission through PET/SiO_x composites increases as the barrier quality

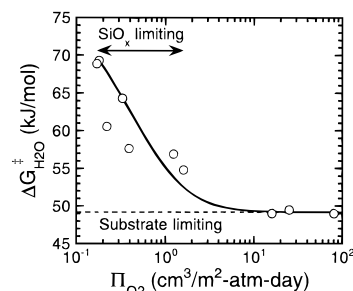
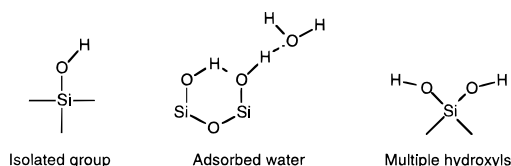


Figure 8. Dependence of the activation energy for H₂O transport ($\Delta G^\ddagger_{H_2O}$) on SiO_x barrier performance (denoted here by the O₂ transmission rate, Π_{O_2} , evaluated at 30 °C). Note that, according to the data listed in Table 2, $\Delta G^\ddagger_{O_2}$ does not depend on Π_{O_2} . The solid line serves as a guide for the eye, whereas the dashed horizontal line identifies the PET substrate limit.

improves. This relationship is displayed in Figure 8, in which $\Delta G^\ddagger_{H_2O}$ is presented as a function of Π_{O_2} on semilogarithmic coordinates. Our reason for using Π_{O_2} as the independent variable is because oxygen behaves as a nearly ideal penetrant that is expected to show very little (if any) physicochemical interaction with the SiO_x surface. Thus, the Π_{O_2} data represent a reliable measure of barrier performance in the present study. According to Figure 8, $\Delta G^\ddagger_{H_2O}$ does not change appreciably for the poor composite barriers relative to PET ($\Delta G^\ddagger_{H_2O} = 50$ kJ/mol). At values of $\Pi_{O_2} < 1$ $\text{cm}^3/\text{m}^2\text{-atm-day}$, however, $\Delta G^\ddagger_{H_2O}$ clearly increases with decreasing Π_{O_2} (by up to about 20 kJ/mol for $10\times$ improved barrier performance). This result questions the role of the SiO_x matrix, which appears to become the permeation-limiting step, in the H₂O transport mechanism. As mentioned earlier with regard to O₂ permeation, it is plausible that the nanoscale defects in the SiO_x coatings with $\Pi_{O_2} < 1$ $\text{cm}^3/\text{m}^2\text{-atm-day}$ are sufficiently small to physically hinder the diffusion of H₂O molecules. In the case of H₂O, however, an additional possibility must be considered: the water molecules may chemically interact with the SiO_x surface. In either case, additional energy would be required for the water molecules to continue permeating.

As reported^{23,25} previously and substantiated here, permeation of small molecules through PECVD-deposited SiO_x coatings is defect-driven. Consider as an extreme case, silica (SiO₂) glass, which exhibits superior barrier properties due to highly constricted interstitial spaces in the Si–O lattice (the Si–O bond length is 0.15 nm). In this case, $\Delta G^\ddagger_{H_2O}$ is about 84 kJ/mol for water vapor permeation through the matrix at elevated temperatures.⁴¹ Because $\Delta G^\ddagger_{H_2O}$ increases by at most 20 kJ/mol beyond that of the PET substrate in Figure 8, the rate-limiting mechanism of water vapor transport in the present SiO_x coatings is not the same as in SiO₂. This difference does not, however, preclude the possibility that the size or shape of the nanoscale defects in the best SiO_x coatings physically hinders the diffusion of H₂O molecules. Another plausible explanation for the observed increase in $\Delta G^\ddagger_{H_2O}$ with decreasing Π_{O_2} is water molecules chemically interacting with the SiO_x surface, especially in confined nanoscale environments. Studies of silica glass have shown³⁴ that dangling bonds (e.g., Si–O– or Si–) rapidly react with water to form SiOH groups. In addition, examination of the hydroxyl population on silica surfaces by infrared spectroscopy^{42,43} suggests that even molecular water physically adsorbs to SiO₂ in abundance. Hydrogen bonding between hydroxyl groups and silica can result in several different arrangements,³⁴ depicted in Scheme 2. Energy penalties required to distort a hydrogen bond arising from hydroxyl/silica coupling range from about 4 to 25 kJ/mol,⁴⁴ which coincides remarkably well with the $\Delta G^\ddagger_{H_2O}$ increase seen in Figure 8. In light of these

SCHEME 2



considerations, we propose that the observed increase in $\Delta G^\ddagger_{\text{H}_2\text{O}}$ with decreasing Π_{O_2} is most likely due to the energy required to remove adsorbed water molecules from the walls of the nanoscale pores, although size-induced hindered diffusion should not be completely ruled out. Further microchemical analysis is necessary to decouple the relative importance of these two effects.

An alternative analysis of the ΔG^\ddagger data obtained during the course of this study for both oxygen and water vapor permeation assists in elucidating the defect density of the SiO_x coatings. Since ΔG^\ddagger for an isothermal process can generally be written as $\Delta H^\ddagger - T\Delta S^\ddagger$, eq 1 may be rewritten as

$$\Pi = \Pi_0 \exp(\Delta S^\ddagger/R) \exp(-\Delta H^\ddagger/RT) \quad (2)$$

In the preceding discussion, the $\Pi_{\text{O}_2}(T)$ and $\Pi_{\text{H}_2\text{O}}(T)$ data shown in Figures 7a and 7b, respectively, have been examined in terms of an Arrhenius-type equation (eq 1). According to eq 2, however, the slopes yielding values of ΔG^\ddagger actually provide only the enthalpic contribution (ΔH^\ddagger), which can be envisaged here as an interaction energy describing the coupled effect of diffusion and solubility of the penetrant molecules in PET and/or SiO_x . [Decoupling these contributions is not possible in the present study.] The corresponding entropic term (ΔS^\ddagger), on the other hand, characterizes the degree of disorder in the matrix and therefore provides a direct measure of the defect (pore) size/density. Although TEM micrographs such as those displayed in Figure 6 reveal that the pore size and population (density) decrease with decreasing Π_{O_2} , a quantitative correlation founded on the basis of such visual investigation would necessarily require analysis of numerous images to ensure statistical meaningfulness. This complication can be avoided through the use of ΔS^\ddagger . Since ΔS^\ddagger cannot be distinguished from the preexponential factor (Π_0), we define ψ_0 as the product $\Pi_0 \exp(\Delta S^\ddagger/R)$ and examine the dependence of this term on barrier performance. It should be noted at this juncture that a similar approach, termed *entropic selectivity*, has been proposed by Singh and Koros⁴⁵ to describe the separation effectiveness of different types of gas membranes.

Extrapolation of the semilogarithmic regressions to $T \rightarrow \infty$ ($T^{-1} \rightarrow 0$) in Figure 7a for oxygen permeation yields the values of ψ_0 presented as a function of barrier efficacy (Π_{O_2} evaluated at 30 °C) in Figure 9. This figure shows that, despite limited experimental scatter attributed to different deposition conditions, an increase in Π_{O_2} generally promotes an increase in ψ_0 . Because the variation in $\Delta H^\ddagger_{\text{O}_2}$ corresponding to oxygen transport in the SiO_x matrix is negligible (recall that $\Delta G^\ddagger_{\text{O}_2}$ is independent of Π_{O_2} from the data provided in Table 2), the increase in ψ_0 with increasing Π_{O_2} confirms the existence of a correlation solely between defect size/density and barrier performance. Recall that the SiO_x coatings employed to generate the $\Pi_{\text{O}_2}(T)$ data for oxygen permeation in Figure 7a have also been employed to obtain the $\Pi_{\text{H}_2\text{O}}(T)$ data in Figure 7b. In this case, the defect size/density information embedded in ψ_0 can be used to elucidate the barrier mechanism of these SiO_x coatings to water vapor. Values of $\Delta G^\ddagger_{\text{H}_2\text{O}}$ (or, alternatively, $\Delta H^\ddagger_{\text{H}_2\text{O}}$) in Figure 8 increase with decreasing Π_{O_2} , whereas the

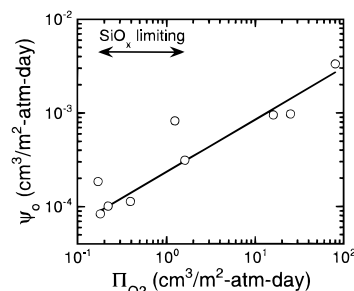


Figure 9. Variation of $\psi_0 [= \Pi_0 \exp(\Delta S^\ddagger/R)]$ for O_2 permeation with SiO_x barrier performance (Π_{O_2} at 30 °C), suggesting a correlation between ΔS^\ddagger , a measure of defect size/density, and barrier quality. The solid line serves as a guide for the eye.

ψ_0 data in Figure 9 increase with increasing Π_{O_2} . It immediately follows that $\Delta G^\ddagger_{\text{H}_2\text{O}}$ (or $\Delta H^\ddagger_{\text{H}_2\text{O}}$) must increase with decreasing ψ_0 , indicating that energetic interactions between the H_2O penetrant molecules and the matrix (PET and/or SiO_x) become more pronounced, due to either physical or chemical considerations, as the size/density of nanoscale defects in the SiO_x matrix decreases.

Conclusions

In this study, the morphological characteristics and barrier efficacy of a large number of PET/ SiO_x composites with SiO_x coatings (deposited from Magnetron-PECVD) widely ranging in oxygen and water vapor barrier quality have been examined to identify key correlations and explore the molecular mechanism by which oxygen and water vapor permeate through such composites. A statistical experimental design employing NPRSM constitutes an efficient optimization algorithm that identifies the optimum conditions of important PECVD process parameters to produce coatings exhibiting superlative barrier performance. Preparation of SiO_x coatings from HMDSO and TMS monomers near optimum deposition conditions yields PET/ SiO_x composites with comparable barrier efficacy. This observation indicates that the use of different organosilicon monomers in SiO_x deposition (by at least Magnetron-PECVD) does not significantly alter the resultant barrier performance.

Images from AFM reveal that the particle shape (i.e., surface texture) and topography of SiO_x coatings vary in a consistent manner as the coating barrier quality is diminished. Good barriers are characterized by the presence of densely packed, small SiO_x grains with a smooth surface. As the barrier performance degrades, the grains become irregularly shaped and coalesce into larger features, producing rougher surfaces and creating more defect sites. Planar TEM images of SiO_x coatings facilitate comparison of microstructure and defect size/density between coatings differing in barrier quality. Intergranular defects typically measuring 4–6 nm across have been detected from such TEM images. No such defects of this nature are evident in good SiO_x coatings. As the barrier quality decreases, the change in particle shape from spherical to irregular promotes an increase in the size/density of nanoscale defect (pore) sites.

The principal mechanism of O_2 and H_2O transport through SiO_x -coated PET occurs through nanoscale defects in the SiO_x coating, followed by activated transport through the PET matrix. Transmission measurements obtained as a function of temperature for both O_2 and H_2O permeation reveal that SiO_x coatings become rate-limiting for both permeant species as the quality of the coatings improves. In the latter case, the activation energy is found to increase by as much as 20 kJ/mol beyond that attributable to permeation through the semicrystalline PET matrix. This increase most likely reflects a combination of

physically constrained H₂O molecules and chemically interacting water molecules (via hydrogen bonding to the SiO_x surface) in defects measuring on the same size scale as the penetrant molecules in good SiO_x barrier coatings. On the basis of this observation, the entropic contribution to the activation energy is adopted as a measure of defect size/density and is found to increase monotonically with decreasing barrier efficacy.

Acknowledgment. Researchers at North Carolina State University are sincerely grateful to Becton Dickinson Technologies for supporting this work and for permitting access to their facilities.

References and Notes

- (1) Krug, T.; Ludwig, R.; Steiniger, G. *SVC 36th Annu. Technol. Conf. Proc.* **1993**, 302.
- (2) Chahroudi, D. *SVC 31st Annu. Technol. Conf. Proc.* **1988**, 145; *SVC 32nd Annu. Technol. Conf. Proc.* **1989**, 29; *SVC 34th Annu. Technol. Conf. Proc.* **1991**, 130.
- (3) Krug, T. G. *SVC 33rd Annu. Technol. Conf. Proc.* **1990**, 163.
- (4) Jamieson, E. H. H.; Windle, A. H. *J. Mater. Sci.* **1983**, 18, 64.
- (5) Misiano, C.; Simonetti, E.; Stafetti, F.; Taglioni, G. *Proc. 6th Internatl. Conf. Vac. Web Coat.* **1992**, Bakish Materials Corp., Englewood, NJ, 70. Misiano, C.; Simonetti, E.; Cerolini, P.; Stafetti, F.; Taglioni, G.; Pasqui, A.; Fusi, F. *SVC 36th Annu. Technol. Conf. Proc.* **1993**, 307.
- (6) Philips, R. W.; Markantes, T.; LeGallee, C. *SVC 36th Annu. Technol. Conf. Proc.* **1993**, 293.
- (7) Bodino, F.; Baud, G.; Benmalek, M.; Besse, J. P.; Dunlop, H. M.; Jacquet, M. *Thin Solid Films* **1994**, 241, 21.
- (8) Felts, J. T.; Grubb, A. D. *J. Vac. Sci. Technol. A* **1992**, 10, 1675.
- (9) Langowski, H. C. *SVC 39th Annu. Technol. Conf. Proc.* **1996**, 398.
- (10) Mercea, P. V.; Bartan, M. *J. Membr. Sci.* **1991**, 59, 353.
- (11) Felts, J. T. *SVC 33rd Annu. Technol. Conf. Proc.* **1990**, 184.
- (12) Nelson, R. J. *SVC 35th Annu. Technol. Conf. Proc.* **1992**, 75.
- (13) Knoll, R. W.; Theil, J. A. *SVC 38th Annu. Technol. Conf. Proc.* **1995**, 425.
- (14) Jansen, F. American Vacuum Society Short Course Program, 43rd National Symposium, American Vacuum Society, Philadelphia, 1996.
- (15) Vossen, J.; Kern, W., Eds., *Thin Film Processes II*, Academic: Boston, 1991; pp 443–496.
- (16) Garcia-Ayuso, G.; Vazquez, L.; Martinez-Duart, J. M. *Surf. Coat. Technol.* **1996**, 80, 203.
- (17) Barker, C. P.; Kochem, K. H.; Revell, K. M.; Kelly, R. S. A.; Badyal, J. P. S. *Thin Solid Films* **1995**, 46, 259.
- (18) Mallik, R. R.; Henriksen, P. N.; Butler, T.; Kulnis, W. J.; Confer, T. J. *J. Vac. Sci. Technol. A* **1992**, 10, 2412.
- (19) Wang, B.-C.; Erlat, A. G.; Spontak, R. J.; Tropsha, Y. G.; Vogler, E. A.; Dalvie, M.; Mar, K. *ACS Polym. Prepr.* **1997**, 38, 1018. Wang, B.-C.; Tropsha, Y.; Montgomery, D. B.; Vogler, E. A.; Spontak, R. J. *J. Mater. Sci. Lett.* **1999**, 18, 311.
- (20) Benmalek, M.; Dunlop, H. M. *Surf. Coat. Technol.* **1995**, 76, 821.
- (21) Thyen, R.; Weber, A.; Klages, C. P. *Surf. Coat. Technol.* **1997**, 97, 26.
- (22) Philips, R. W.; Markantes, T.; LeGallee, C. *SVC 36th Annu. Technol. Conf. Proc.* **1993**, 293.
- (23) Roberts, A. P.; Henry, B. M.; Sutton, A. P.; Grovenor, C. R. M.; Briggs, G. A. D. (submitted for publication).
- (24) Henry, B. M.; Roberts, A. P.; Grovenor, C. R. M.; Sutton, A. P.; Briggs, G. A. D.; Tsukahara, Y.; Miyamoto, Y. M.; Chater, R. J. *SVC 41st Annu. Technol. Conf. Proc.* **1998**, 434.
- (25) Tropsha, Y. G.; Harvey, N. G. *J. Phys. Chem. B* **1997**, 101, 2239.
- (26) Haaland, P. D.; Clarke, R.; O'Connell, M.; Baik, J.; Hardy, S.; Nychka, D. Non-Parametric Response Surface Methods, **1997**, presented at Workshop on Topics in Model Fitting and Mixture Experiments, Irsee, Germany.
- (27) Yasuda, H. *Plasma Polymerization*, Academic: New York, 1985; pp 277–333.
- (28) Martin, Y.; Williams, C. C.; Wichramasinghe, G. H. *Appl. Phys.* **1987**, 61, 4723.
- (29) Reimer, L., Ed., *Energy-Filtering Transmission Electron Microscopy*; Springer-Verlag: New York, 1995.
- (30) Williams, J. L.; Burkett, S. L.; McGuire, S. U.S. Patent 5,364,666, 15 November 1994.
- (31) Green, P. J.; Silverman, B. W. *Nonparametric Regression and Generalized Linear Models*, Chapman and Hall: London, 1994.
- (32) Lee, J. H.; Kim, D. S.; Lee, Y. H. *J. Electrochem. Soc.* **1996**, 143, 1442.
- (33) Theil, J. A.; Brace, J. G.; Knoll, R. W. *J. Vac. Sci. Technol. A* **1994**, 12, 1365.
- (34) Doremus, R. H. *Glass Science*, John Wiley & Sons: London, 1973.
- (35) Michalske, T. A.; Bunker, B. C. *Sci. Am.* **1987**, 257, 122.
- (36) Robinson, G. W.; Zhu, S.-B.; Singh, S.; Evans, M. W. *Water in Biology, Chemistry and Physics*; World Scientific: Singapore, 1996.
- (37) Perkins, W. G.; Begeal, D. R. *J. Chem. Phys.* **1971**, 54, 1683.
- (38) Norton, F. J. *J. Am. Ceram. Soc.* **1953**, 36, 90.
- (39) Stannet, V. In *Diffusion in Polymers*; Crank, J. Ed.; Academic: New York, 1968, pp 41–73.
- (40) Erlat, A. G.; Wang, B.-C.; Spontak, R. J.; Tropsha, Y.; Mar, K. D.; Montgomery, D. B.; Vogler, E. A. submitted for publication in *J. Mater. Res.*
- (41) Moulson, J.; Roberts, T. P. *Trans. Faraday Soc.* **1961**, 57, 1208.
- (42) McDonald, R. S. *J. Phys. Chem.* **1958**, 62, 1168.
- (43) Little, L. H. *Infrared Spectra of Adsorbed Species*, Academic: London, 1966.
- (44) Eisenberg, D.; Kauzmann, W. *The Structure and Properties of Water*, Clarendon: Oxford, 1969; p 179.
- (45) Singh, A.; Koros, W. J. *Ind. Eng. Chem. Res.* **1996**, 35, 1231.